

# Prediction of Novel 2D Intrinsic Ferromagnetic Materials with High Curie Temperature and Large Perpendicular Magnetic Anisotropy

Ruilin Han,\* Zhou Jiang, and Yu Yan



Cite This: <https://dx.doi.org/10.1021/acs.jpcc.0c01307>



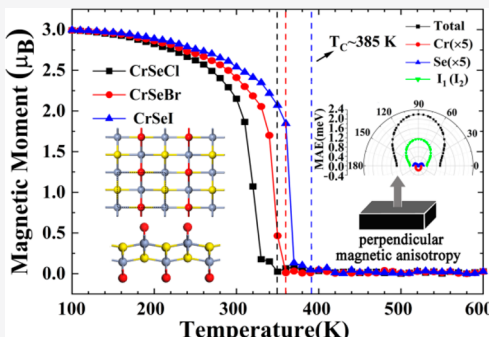
Read Online

ACCESS |

Metrics & More

Article Recommendations

**ABSTRACT:** Two-dimensional intrinsic ferromagnets with high Curie temperature and large perpendicular magnetic anisotropy (PMA) are promising candidates for data storage and spintronics applications. In this work, first-principle calculations and Monte Carlo simulation are used to investigate the stability, electronic structure, and magnetic anisotropy of monolayers of CrSeX ( $X = \text{Cl}, \text{Br}, \text{I}$ ). It is found that monolayer CrSeX ( $X = \text{Cl}, \text{Br}, \text{I}$ ) species are two-dimensional intrinsic ferromagnets and are thermally stable at room temperature. It is worth noting that the Curie temperatures of monolayer CrSeX ( $X = \text{Cl}, \text{Br}, \text{I}$ ) can reach or even exceed room temperature, and a strong PMA can be obtained in monolayer CrSeI. Interestingly, the PMA of monolayer CrSeI is mainly provided by the nonmetallic I atom with large spin-orbit coupling and magnetic anisotropy of the nonmetallic I atom reaching up to 0.572 meV/I atom, which is comparable to that of metallic Fe atoms at Fe/MgO interfaces. In contrast to monolayer CrSeI, monolayer CrSeCl and CrSeBr possess weak in-plane magnetic anisotropy, and their easily magnetized direction is the [100] axis. By analyzing the projected density of states and the p-orbital-resolved magnetic anisotropy energy of the nonmetallic I atom based on second-order perturbation theory, we find that the large PMA of monolayer CrSeI is mainly provided by the matrix element difference between the spin-up  $p_x$  and  $p_y$  states of the nonmetallic I atoms, and the difference between it and the matrix element difference between the spin-up  $p_y$  and  $p_z$  states of the nonmetallic I atoms in the case of the magnetic moment aligning [100] and [010] axes is the reason why the energy of monolayer CrSeI for the magnetic moment aligning [100] axis is smaller than the energy for the magnetic moment aligning [010] axis. This study suggests that monolayer CrSeI is a promising candidate for future applications in spintronic devices.



## 1. INTRODUCTION

As a platform to study novel physical phenomena, two-dimensional (2D) magnetic materials have attracted research interest worldwide. Most currently known 2D materials, including graphene,<sup>1</sup> phosphine,<sup>2</sup> and MoS<sub>2</sub>,<sup>3</sup> do not possess intrinsic ferromagnetism, which limits their usefulness for spintronic devices. Although magnetic properties can, in principle, be introduced into nonmagnetic materials by doping magnetic atoms, producing defects, or using the interfacial proximity effect, the introduced magnetic properties are sensitive to the precise control of these strategies in experiments.<sup>4–10</sup> For this reason, it is preferable and desirable to find 2D materials with intrinsic ferromagnetism.

According to the Mermin–Wagner theorem,<sup>11</sup> thermal fluctuations may easily destroy 2D magnetism in the isotropic Heisenberg model at finite temperatures. However, magnetic anisotropy can remove this limitation, thus allowing one to obtain 2D intrinsic ferromagnets. Therefore, magnetic anisotropy is the key factor for 2D intrinsic ferromagnetism. In 2017, 2D intrinsic ferromagnets, including monolayer CrI<sub>3</sub> and bilayer Cr<sub>2</sub>Ge<sub>2</sub>Te<sub>6</sub>, were discovered experimentally.<sup>12,13</sup> Because 2D materials can be regarded as atomically thin films,

2D intrinsic ferromagnets with large perpendicular magnetic anisotropy (PMA) are promising candidates suitable for application in high-density magnetic storage. Meanwhile, magnetic tunnel junctions (MTJs) with PMA are beneficial for obtaining sufficiently high thermal stability and low critical switching current in nonvolatile magnetic random-access memories. As a result, much effort has been invested to investigate the PMA of 2D intrinsic ferromagnets, heterostructures, and MTJs.<sup>14–27</sup> As known, lower Curie temperatures of monolayer CrI<sub>3</sub> and bilayer Cr<sub>2</sub>Ge<sub>2</sub>Te<sub>6</sub> limit their application in high-density magnetic storage and spintronic devices. Hence, it is desirable to search for 2D intrinsic ferromagnets with high Curie temperature. In this regard, some 2D intrinsic ferromagnets with high Curie-temperature, such as

Received: February 14, 2020

Revised: March 21, 2020

$\text{VTe}_2$ ,  $\text{VSe}_2$ ,  $\text{Fe}_3\text{GeTe}_2$ ,  $\text{MnSe}_x$ , and 1T- $\text{CrTe}_2$ , were prepared using molecular beam epitaxial growth, chemical vapor phase, or mechanical exfoliation.<sup>7,10,28–32</sup> On the other hand, a series of 2D monolayer intrinsic ferromagnetic materials with Curie temperature higher than  $\text{CrI}_3$  were theoretically predicted, including:  $\text{ScCl}$  (185 K),<sup>33</sup>  $\text{MX}_2$  ( $\text{M} = \text{Fe}, \text{Co}, \text{Ni}; \text{X} = \text{Cl}, \text{Br}, \text{I}$ ) (80–200 K),<sup>34,35</sup>  $\text{CrSX}$  ( $\text{X} = \text{Cl}, \text{Br}, \text{I}$ ) (150–300 K),<sup>36–38</sup>  $\text{LaBr}_2$  (270 K),<sup>36</sup>  $\text{RuI}_3$  (360 K),<sup>38</sup>  $\text{CrOX}$  ( $\text{X} = \text{Cl}, \text{Br}$ ) (160 and 129 K),<sup>39</sup>  $\text{MO}_2$  ( $\text{M} = \text{Ru}, \text{Os}$ ) (38 and 197 K),<sup>40</sup>  $\text{Cr}_3\text{X}_4$  ( $\text{X} = \text{Se}, \text{Te}$ ) (370 and 460 K),<sup>41</sup>  $\text{Fe}_3\text{P}$  (420 K),<sup>42</sup>  $\text{TMX}_3$  ( $\text{TM} = \text{Ti}, \text{V}; \text{X} = \text{Cl}, \text{I}$ ) (80–425 K),<sup>43,44</sup>  $\text{MoN}_2$  (420 K),<sup>45</sup>  $\text{MnN}$  (368 K),<sup>46</sup>  $\text{MnP}$  (495 K),<sup>47</sup>  $\text{FeCl}_2$ ,<sup>48</sup> and  $\text{CrSI}$ .<sup>49</sup> Among these 2D intrinsic ferromagnets with high Curie temperature, only monolayer  $\text{MO}_2$  ( $\text{M} = \text{Ru}, \text{Os}$ ),  $\text{Fe}_3\text{P}$ ,  $\text{MnP}$ ,  $\text{FeCl}_2$ , and  $\text{CrSI}$  possess large PMA. To date, no 2D intrinsic ferromagnets with high Curie temperature and large PMA energy has been reported experimentally.

This article systematically studies the stability, electronic structure, and magnetic anisotropy of monolayer  $\text{CrSeX}$  ( $\text{X} = \text{Cl}, \text{Br}, \text{I}$ ) and predicts the Curie temperature of monolayer  $\text{CrSeX}$  ( $\text{X} = \text{Cl}, \text{Br}, \text{I}$ ) by using first-principle calculations and Monte Carlo (MC) simulations. Monolayer  $\text{CrSeX}$  ( $\text{X} = \text{Cl}, \text{Br}, \text{I}$ ) is predicted to be a 2D intrinsic ferromagnet with Curie temperature above room temperature. More remarkably, the calculated PMA energy of monolayer  $\text{CrSeI}$  is as high as 0.572 meV per nonmetallic I atom and the large PMA of monolayer  $\text{CrSeI}$  mainly originates from the spin-polarized p-orbitals of the nonmetallic I atoms. Based on second-order perturbation theory, it is found that the large PMA energy of monolayer  $\text{CrSeI}$  is mainly provided by the matrix element difference between spin-up  $p_x$  and  $p_y$  orbitals of the I atom.

## 2. COMPUTATIONAL METHODS

All calculations were performed on the basis of density functional theory (DFT) framework with the Perdew–Burke–Ernzerhof (PBE) functional in the generalized gradient approximation as implemented in the Vienna ab initio simulation package (VASP).<sup>50,51</sup> In this paper, the GGA + U method<sup>52</sup> is used to consider the correlation effect of 3d electrons in Cr, and the Coulomb interaction parameter U of the Cr 3d electrons was assumed as 3.0 eV, which is consistent with previously reported values.<sup>36,37,49,53,54</sup> The cutoff energy of the planar-wave basis set was set to 500 eV. The integration at the Brillouin zone special point was performed using the gamma-centered Monkhorst–Pack method.<sup>55</sup> The k-point grid was optimized by testing convergence of anisotropy energy of the monolayer  $\text{CrSeX}$  ( $\text{X} = \text{Cl}, \text{Br}, \text{I}$ ) and the optimized k-point value was  $27 \times 21 \times 1$ . The structure of monolayer  $\text{CrSeX}$  ( $\text{X} = \text{Cl}, \text{Br}, \text{I}$ ) was fully relaxed, and the convergence precision of energy and force were  $10^{-7}$  eV and  $10^{-3}$  eV/Å, respectively. A vacuum layer of 20 Å in the direction perpendicular to the monolayer  $\text{CrSeX}$  ( $\text{X} = \text{Cl}, \text{Br}$  and  $\text{I}$ ) was used to prevent interaction between periodic lattices.

The phonon-spectrum calculation was carried out using the Phonopy package through density functional perturbation theory.<sup>56</sup> Here a  $3 \times 3 \times 1$  supercell (containing 54 atoms) was used for phonon-spectrum calculation, and a  $9 \times 7 \times 1$  Monkhorst–Pack k-point grid was used to integrate the Brillouin zone. Ab-initio molecular dynamics simulation at 300 K was performed using the canonical ensemble (NVT), which lasted for a total of 8.0 ps at a step size of 1.0 fs. The temperature of 300 K was controlled by using the Nosé–Hoover method.<sup>57</sup>

Monte Carlo simulations, based on the 2D Heisenberg model, were used to evaluate the Curie temperature of monolayer  $\text{CrSeX}$  ( $\text{X} = \text{Cl}, \text{Br}, \text{I}$ ) ferromagnets. The corresponding spin Hamiltonian is expressed as

$$\mathbf{H} = - \sum_{ij} J_1 S_i S_j - \sum_{kl} J_2 S_k S_l \quad (1)$$

where  $J_1$  and  $J_2$  represent the nearest-neighbor and next-nearest-neighbor magnetic interaction parameters, respectively, as shown in Figure 1a, and  $S$  represents the spin vector of each

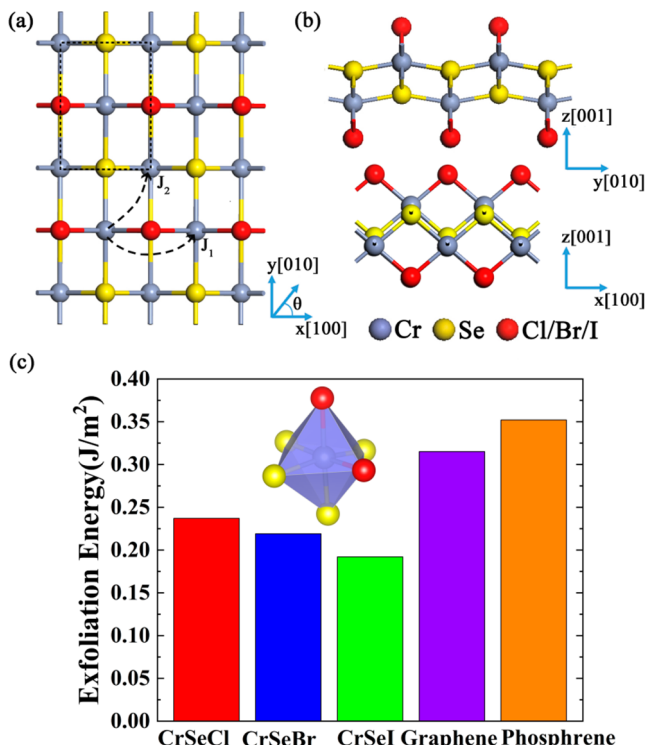


**Figure 1.** Top (a) and side (b) views of the crystal structure of monolayer  $\text{CrSeX}$  ( $\text{X} = \text{Cl}, \text{Br}, \text{I}$ ). The rectangular area surrounded by black dotted lines in panel a represents a unit cell of monolayer  $\text{CrSeX}$  ( $\text{X} = \text{Cl}, \text{Br}, \text{I}$ ); Calculated exfoliation energy (c) of monolayer  $\text{CrSeX}$  ( $\text{X} = \text{Cl}, \text{Br}, \text{I}$ ), graphene, and phosphene and the inset in panel c shows the distorted  $\text{CrSe}_4\text{X}_2$  octahedron.

atom.  $J_1$  and  $J_2$  of monolayer  $\text{CrSeX}$  ( $\text{X} = \text{Cl}, \text{Br}, \text{I}$ ) were calculated from the energy difference between the ferromagnetic (FM) state and two antiferromagnetic (AFM1 and AFM2) states,<sup>58</sup> in which AFM1 and AFM2 states are set in a  $2 \times 1$  supercell. For each monolayer compound, the MC simulation performed  $1.2 \times 10^5$  iterations for a  $120 \times 120 \times 1$  superlattice. According to eq 1, the energy of the FM, AFM1, and AFM2 states follow as

$$E(\text{FM}) = -(4J_1 + 8J_2)|S|^2 \quad (2)$$

$$E(\text{AFM1}) = -(4J_1 - 8J_2)|S|^2 \quad (3)$$

$$E(\text{AFM2}) = -4J_1|S|^2 \quad (4)$$

Then,

$$J_1 = \frac{2\Delta E_2 - \Delta E_1}{16S^2} \quad (5)$$

**Table 1.** Optimized Lattice Constants ( $a$  and  $b$ ), Magnetic Moments of Cr, Se, and X ( $M_{\text{Cr}}$ ,  $M_{\text{Se}}$ ,  $M_{\text{X}}$ ), Nearest and Next-nearest Exchange Coupling Constants ( $J_1$  and  $J_2$ ), Energy Difference ( $E_{\text{FM}-\text{AFM}}$ ) between the Ferromagnetic States (FM) and the Lowest Antiferromagnetic (AFM) States, and Optimized Cr–Se–Cr and Cr–X–Cr Angles for Monolayer CrSeX (X = Cl, Br, I)

system	$a$ (Å)	$b$ (Å)	$M_{\text{Cr}}$ ( $\mu_{\text{B}}$ )	$M_{\text{Se}}$ ( $\mu_{\text{B}}$ )	$M_{\text{X}}$ ( $\mu_{\text{B}}$ )	$J_1$ (meV)	$J_2$ (meV)	$E_{\text{FM}-\text{AFM}}$ (meV/unit cell)	$\theta_1$ (deg)	$\theta_2$ (deg)	$\theta_3$ (deg)
CrSeCl	3.582	5.167	3.424	-0.314	-0.064	1.058	1.423	-178.693	89.626	95.984	96.717
CrSeBr	3.681	5.122	3.447	-0.318	-0.089	1.362	1.419	-200.351	92.306	92.147	96.982
CrSeI	3.852	5.102	3.382	-0.293	-0.115	1.512	1.485	-209.709	95.693	88.611	96.975

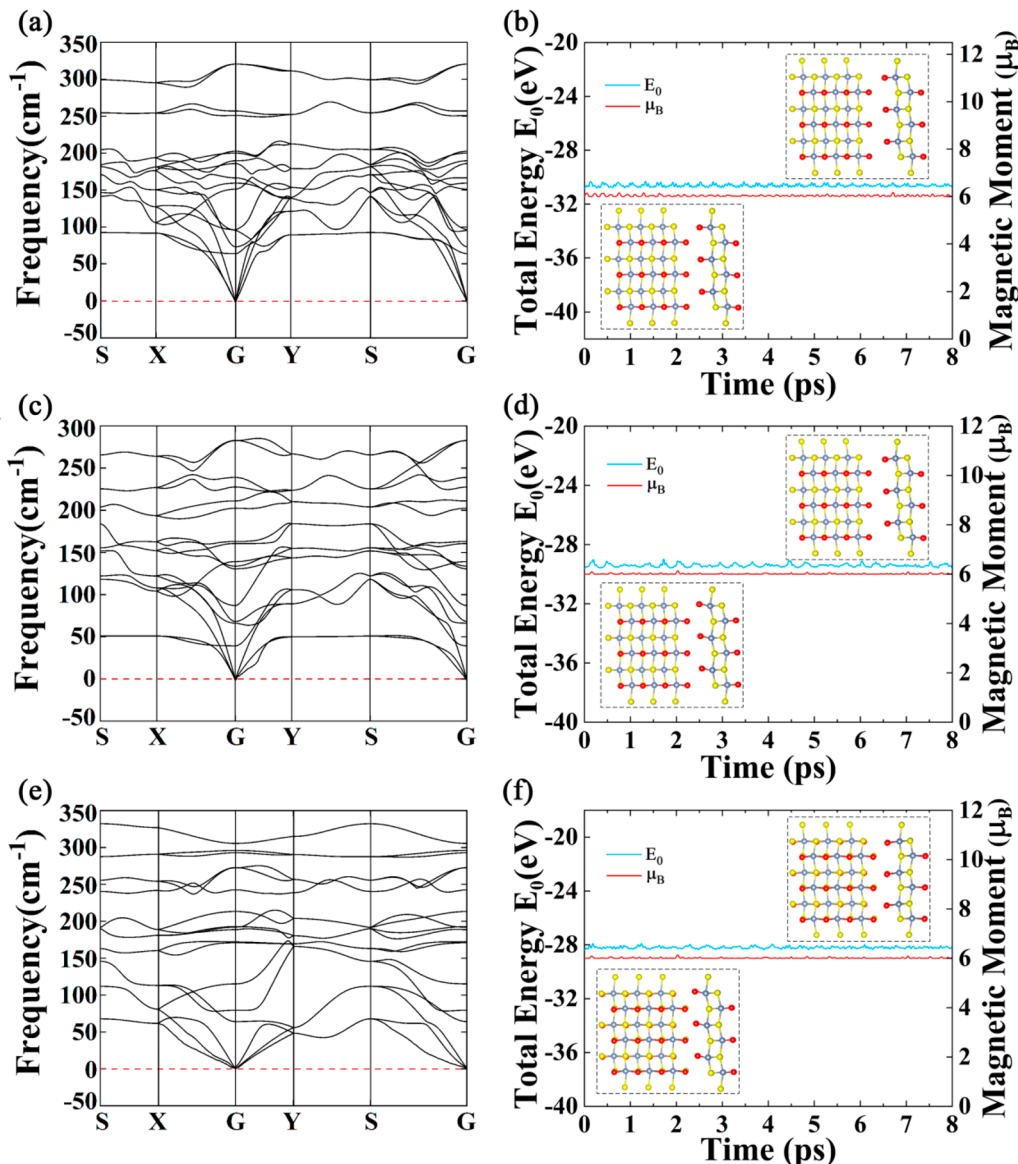


**Figure 2.** Calculated phonon dispersion of monolayer CrSeCl (a), CrSeBr (c), and CrSeI (e), as well as fluctuation of total energy and magnetic moments of monolayer CrSeCl (b), CrSeBr (d), and CrSeI (f) during the AIMD simulation. The insets in panels b, d, and f show structural snapshots of monolayer CrSeX (X = Cl, Br, I) at 4 and 8 ps, respectively. The gray, yellow, and red balls represent Cr, Se, and X atoms, respectively.

$$J_2 = \frac{\Delta E_1}{16S^2} \quad (6)$$

where  $\Delta E_1$  is the energy difference between the AFM1 and FM states and  $\Delta E_2$  is the energy difference between the AFM2 and FM states.

The magnetic anisotropy energy (MAE) of monolayer CrSeX (X = Cl, Br, I) was calculated using the torque method,<sup>59,60</sup> in which the spin–orbit coupling (SOC) was

treated as the perturbation term. The MAE of monolayer CrSeX (X = Cl, Br, I) is defined as  $\text{MAE} = E_{\theta} - E_z$ , where  $E_{\theta}$  and  $E_z$  represent the total energy with the magnetic moment along the in-plane axis and the out-of-plane  $z$  axis, respectively, and angle  $\theta$  represents the angle between one in-plane ( $xy$  plane) magnetized axis and  $x$  ([100]) axis, as shown in Figure 1a. This way, depending on whether the MAE is positive or negative, it can be determined whether the easy axis is perpendicular to the plane of CrSeX (X = Cl, Br I). Based on

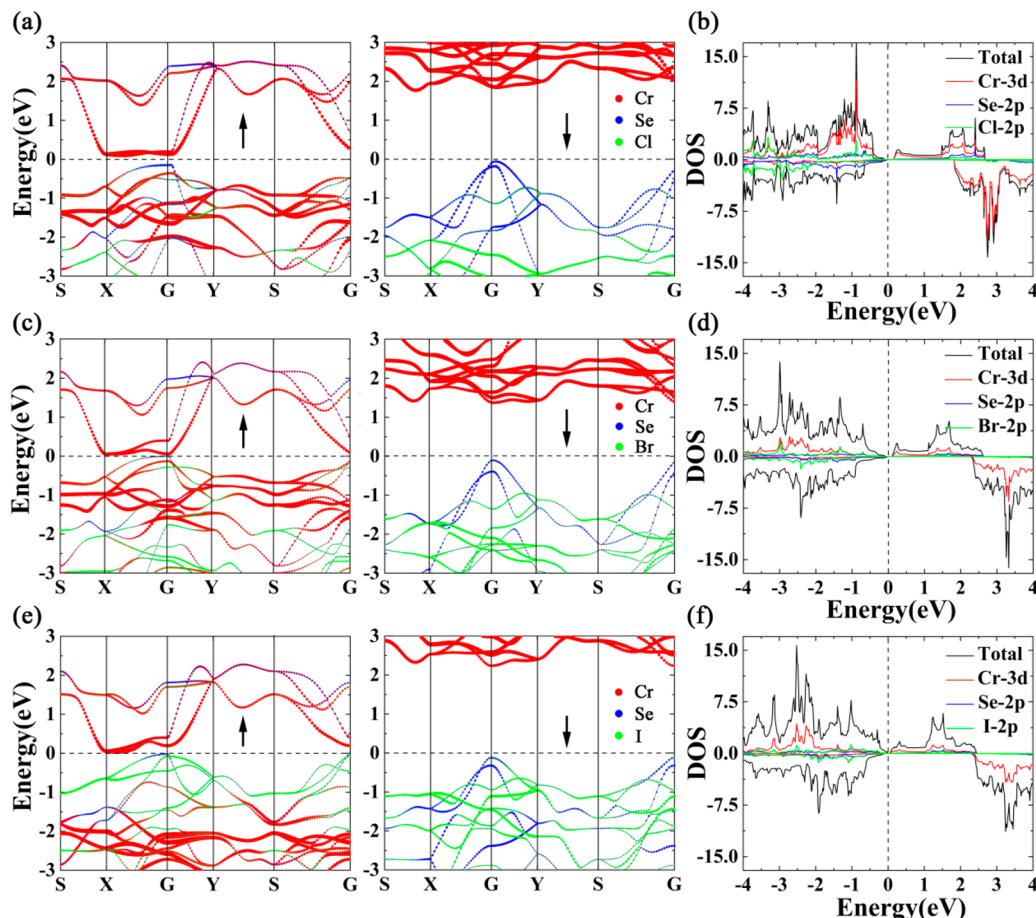


**Figure 3.** Spin-resolved band structure of monolayer CrSeCl (a), CrSeBr (c), and CrSeI (e) with spin-up ( $\uparrow$ ) and spin-down ( $\downarrow$ ). The red, blue, and green dots represent the contribution from Cr, Se, and X atoms, respectively, and the symbol size is proportional to its associated population. Total DOS and partial DOS of p orbitals of the I (Cl or Br) atom, p orbitals of Se atom, and d orbitals of Cr atom for monolayer CrSeCl (b), CrSeBr (d), and CrSeI (f). The Fermi level is set to zero.

second-order perturbation theory,<sup>61</sup> the MAE can be expressed as

$$\text{MAE}_{\theta_z} = \sum_{\sigma\sigma'} E^{\sigma\sigma'}(\theta) - E^{\sigma\sigma'}(z) \\ = \sum_{\sigma\sigma'} (2\delta_{\sigma\sigma'} - 1) \\ \xi^2 \sum_{\sigma, u^\sigma} \frac{|\langle o^\sigma | L_z | u^\sigma' \rangle|^2 - |\langle o^\sigma | L_\theta | u^\sigma' \rangle|^2}{E_u^\sigma - E_o^\sigma} \quad (7)$$

where  $\xi$  denotes the SOC constant and  $E_u^\sigma$  and  $E_o^\sigma$  represent the energy levels of the unoccupied state of spin  $\sigma'$  ( $|u^\sigma'\rangle$ ) and the occupied state of the spin  $\sigma$  ( $|o^\sigma\rangle$ ), respectively. When  $\theta$  is equal to  $0^\circ$ , eq 7 represents a difference in the obtained energies for the magnetic moment aligning in  $x$  ([100]) and  $z$  ([001]) axes. Furthermore, when  $\theta$  is equal to  $90^\circ$ , eq 7 represents a difference in the obtained energies for magnetic moment aligning in  $y$  ([010]) and  $z$  ([001]) axes. The square differences of the orbital-momentum matrix elements in eq 7, that is,  $|\langle o^\sigma | L_z | u^\sigma' \rangle|^2 - |\langle o^\sigma | L_\theta | u^\sigma' \rangle|^2$ , is simply called the matrix element difference and is abbreviated as  $(o^\sigma, u^\sigma')$  in the following discussion.

### 3. RESULTS AND DISCUSSION

The chromium selenium halide CrSeX (X = Cl, Br, I) belongs to the orthorhombic system with  $Pmnmm$  space group. Figure 1a,b shows top and side views of the crystal structure of monolayer CrSeX (X = Cl, Br, I). The rectangular area surrounded by black dotted lines in Figure 1a represents a unit cell of monolayer CrSeX (X = Cl, Br, I), which contains two chromium atoms, two selenium atoms, and two halogen atoms. The inset in Figure 1c shows that Cr is coordinated by four selenium and two halide ions forming a distorted octahedron of  $\text{CrSe}_4\text{X}_2$ .

First, the stability of monolayer CrSeX (X = Cl, Br, I) is studied. The optimized lattice constants  $a$  and  $b$  of monolayer CrSeCl, CrSeBr, and CrSeI are 3.582 and 5.167, 3.681 and 5.122, and 3.852 and 5.102 Å, respectively (see Table 1). The optimized lattice parameters for monolayer CrSeBr are generally consistent with a previous theoretical result.<sup>36</sup> Although monolayer CrSeX (X = Cl, Br, I) has not been experimentally prepared, the bulk CrSBr was already synthesized, and it was reported to be layered van der Waals crystals.<sup>62,63</sup> Here we simulate the exfoliation process and predict the exfoliation energy of monolayer CrSeX (X = Cl, Br, I) using a rigorous method.<sup>64</sup> Figure 1c shows that the calculated exfoliation energies of graphene and phosphene are 0.315 and 0.352 J/m<sup>2</sup>, respectively, which agrees well with experimental measurements and other theoretically reported values.<sup>65,66</sup> For

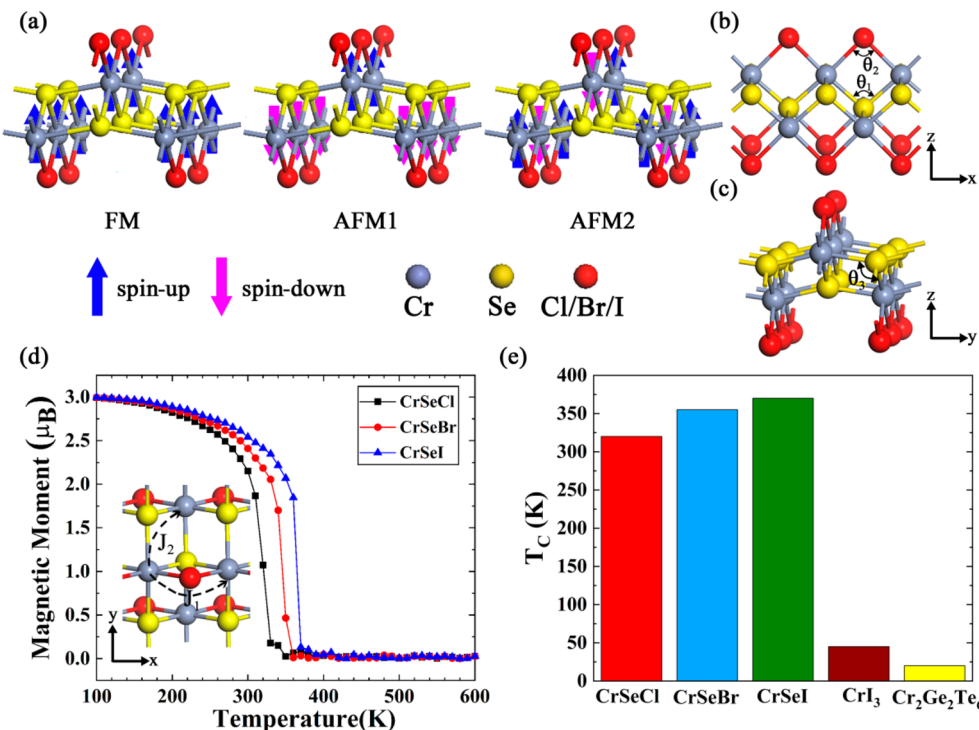


**Figure 4.** The  $2 \times 1$  supercell (a) of monolayer CrSeX ( $X = \text{Cl}, \text{Br}, \text{I}$ ) with initial magnetic moment settings for the FM, AFM1, and AFM2 states. The blue and pink arrows represent the spin-up and spin-down magnetic moment of Cr, respectively. Side views (b, c) of the monolayer CrSeX, where the Cr–Se–Cr and Cr–X–Cr angles are labeled as  $\theta_1$ ,  $\theta_2$ , and  $\theta_3$ , respectively. Variation (d) of magnetic moment of monolayer CrSeX ( $X = \text{Cl}, \text{Br}, \text{I}$ ) as a function of the temperature. The inset shows the first ( $J_1$ ) and second ( $J_2$ ) nearest-neighboring exchange interactions for the monolayers CrSeX. Curie temperatures (e) of monolayer CrSeX ( $X = \text{Cl}, \text{Br}, \text{I}$ ) ferromagnets, CrI<sub>3</sub> (45 K), and Cr<sub>2</sub>Ge<sub>2</sub>Te<sub>6</sub> (20 K).

monolayer CrSeX ( $X = \text{Cl}, \text{Br}, \text{I}$ ), the calculated exfoliation energy is much lower than that of graphene. Combined with the earlier reports about synthesis of graphene and phosphene, it is estimated that monolayer CrSeX ( $X = \text{Cl}, \text{Br}, \text{I}$ ) can be prepared from bulk structures.

The stability of a new 2D layered material is very important for practical applications. Therefore, this article further evaluates the stability of monolayer CrSeX ( $X = \text{Cl}, \text{Br}, \text{I}$ ) by performing phonon dispersion calculations and ab initio molecular dynamics simulations. As shown in Figure 2a,c,e, the frequencies of all phonon modes within the entire wave-vector-space are positive, indicating that monolayer CrSeX ( $X = \text{Cl}, \text{Br}, \text{I}$ ) are dynamically stable. Figure 2b,d,f shows the evolution of single-atom average energies and magnetic moments for the monolayer CrSeX ( $X = \text{Cl}, \text{Br}, \text{I}$ ) system during the molecular dynamics simulation. The insets in Figure 2b,d,f show the top and side views of the  $3 \times 3 \times 1$  supercell structure at 4 ps and at the end of molecular dynamics simulation (8 ps). As shown in Figure 2b,d,f, the energy and magnetic moment of monolayer CrSeX ( $X = \text{Cl}, \text{Br}, \text{I}$ ) remain basically stable over the entire molecular dynamics simulation process, and the structure retains its integrity without noticeable distortion until the end of the molecular dynamics simulation. These results indicate that monolayer CrSeX ( $X = \text{Cl}, \text{Br}, \text{I}$ ) is thermally stable at room temperature. Correspondingly, Zhao's groups also reported that the monolayer CrSeBr is thermally stable at room temperature after 10 ps.<sup>36</sup>

Next, the electronic structure and magnetic properties of monolayer CrSeX ( $X = \text{Cl}, \text{Br}, \text{I}$ ) are investigated. The calculation results indicate that the energy differences between the spin-polarized and non-spin-polarized states of monolayer CrSeCl, CrSeBr, and CrSeI are  $-6.49$ ,  $-7.02$ , and  $-7.10$  eV/

unit cell, respectively, which indicatess that the ground state of the system is magnetic. Figure 3 shows the spin-resolved band structure and the spin-polarized density of states (DOS) of monolayer CrSeX ( $X = \text{Cl}, \text{Br}, \text{I}$ ). The calculation results suggest that monolayer CrSeCl and CrSeBr are direct band gap semiconductors with band gaps of 0.142 and 0.105 eV, while monolayer CrSeI is an indirect band gap semiconductor with a band gap of 0.053 eV. Figure 3 shows that the valence-band maximum and conduction-band minimum of the monolayer CrSeCl and CrSeBr are both located at the point G. In contrast, the valence-band maximum of the monolayer CrSeI is located at the point G, while the conduction-band minimum is located at the point X. Moreover, the band gap size of monolayer CrSeX ( $X = \text{Cl}, \text{Br}, \text{I}$ ) decreases with increasing atomic radius of X from Cl to I. In addition, the DOS in Figure 3 shows that the states near the conduction-band minimum of the monolayer CrSeX ( $X = \text{Cl}, \text{Br}, \text{I}$ ) are mainly determined by the d-orbital electrons of the Cr atom. Also, as X changes from Cl to I, the contributions from the p-orbital electrons of the Se atom to the valence-band maximum decrease, while the contributions from the p-orbital electrons of atom X increase. Similar electronic structures also were found in the CrSX ( $X = \text{Cl}, \text{Br}, \text{I}$ ) system and were well explained.<sup>37</sup> It is noticed that the calculated DOS of monolayer CrSeBr agrees well with the result in ref 36. The calculated magnetic moment of monolayer CrSeCl, CrSeBr, and CrSeI are  $3.046$ ,  $3.040$ , and  $2.974 \mu_B/\text{unit cell}$ , respectively. Table 1 shows that the magnetic moment of the monolayer CrSeX ( $X = \text{Cl}, \text{Br}, \text{I}$ ) system is mainly derived from the Cr atoms. The energy differences between the FM state and the AFM state of monolayer CrSeX ( $E_{\text{FM}-\text{AFM}}$ ) are also indexed in Table 1, where the AFM state is the lowest energy state in AFM1 and AFM2 states. As shown in Table 1,

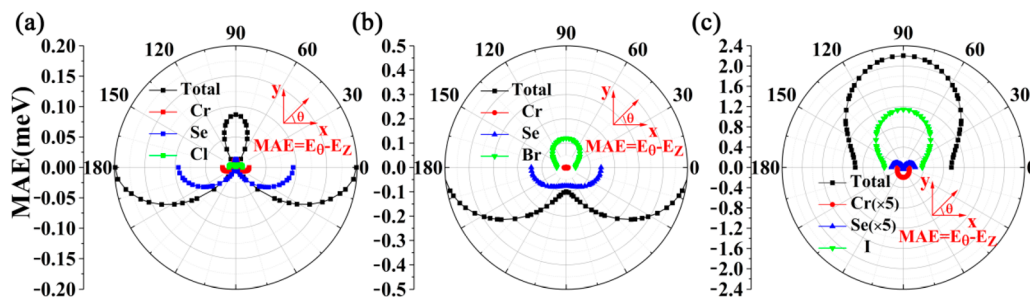


**Figure 5.** Variation of total MAE and MAE of each atom in monolayer CrSeCl (a), CrSeBr (b), and CrSeI (c) as a function of angle  $\theta$  ranging from 0 to  $180^\circ$ .

**Table 2. Atom-Resolved MAE, Total MAE for Angles  $\theta = 0^\circ$  and  $90^\circ$ , and Easy Magnetization Axis (EMA) for the Monolayer CrSeX ( $X = \text{Cl}, \text{Br}, \text{I}$ )**

System	MAE	MAE meV/Cr	MAE meV/Se	MAE meV/X	MAE meV/unit ell	EMA
CrSeCl	$E_{[100]} - E_{[001]}$	-0.011	-0.047	0.006	-0.199	in-plane [100] axis
	$E_{[010]} - E_{[001]}$	0.007	0.006	-0.002	0.087	
CrSeBr	$E_{[100]} - E_{[001]}$	-0.004	-0.072	0.019	-0.504	in-plane [100] axis
	$E_{[010]} - E_{[001]}$	0.001	-0.038	0.060	-0.099	
CrSeI	$E_{[100]} - E_{[001]}$	-0.011	0.023	0.193	0.951	out-of-plane [001] axis
	$E_{[010]} - E_{[001]}$	-0.019	-0.004	0.572	2.206	

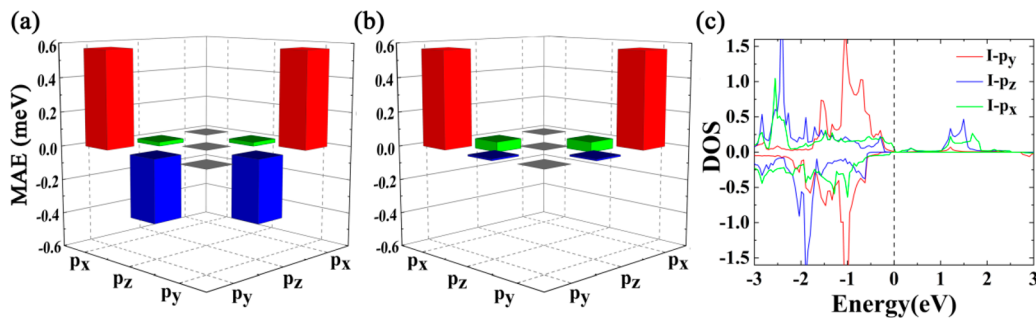


**Figure 6.** p-Orbital-resolved MAE of the nonmetallic I atom in monolayer CrSeI when  $\theta$  is equal to  $0^\circ$  (a) and  $90^\circ$  (b). Partial DOS (c) for the p orbital of the nonmetallic I atom in monolayer CrSeI.

the  $E_{\text{FM-AFM}}$  values of monolayer CrSeCl, CrSeBr, and CrSeI are  $-178.693$ ,  $-200.351$ , and  $-209.709$  meV/unit cell, respectively, which indicates that monolayer CrSeX ( $X = \text{Cl}, \text{Br}, \text{I}$ ) is a 2D intrinsic ferromagnet.

In the following, the Curie temperature of the monolayer ferromagnetic CrSeX ( $X = \text{Cl}, \text{Br}, \text{I}$ ) is estimated using MC simulation. Figure 4a shows the initial magnetic moment settings for the FM, AFM1, and AFM2 states in the  $2 \times 1$  supercell. As shown in Figure 4b,c, there are three different cation–anion–cation bond angles in monolayer CrSeX ( $X = \text{Cl}, \text{Br}, \text{I}$ ), including two Cr–Se–Cr angles ( $\theta_1$  and  $\theta_3$ ) and one Cr–X–Cr angle ( $\theta_2$ ). Our calculations show that  $J_1$  and  $J_2$  of monolayer CrSeCl, CrSeBr, and CrSeI are 1.058 and 1.423 meV, 1.362 and 1.419 meV, and 1.512 and 1.485 meV, respectively, as shown in Table 1, which indicates that the magnetic interactions between two nearest-neighbor Cr atoms and two next-nearest-neighbor Cr atoms are FM. According to the Goodenough–Kanamori–Anderson rule,<sup>67–69</sup> the superexchange interaction between two cations in a system with a cation–anion–cation bond angle of  $\sim 90^\circ$  is FM coupling. Correspondingly, Table 1 shows that the bond angles  $\theta_1$ ,  $\theta_2$ , and  $\theta_3$  in monolayer CrSeCl, CrSeBr, and CrSeI are almost equal to or close to  $90^\circ$ . Therefore,  $J_1$  and  $J_2$  of monolayer CrSeCl, CrSeBr, and CrSeI are positive. Furthermore, Figure

4d shows the variation of magnetic moment of monolayer CrSeX ( $X = \text{Cl}, \text{Br}, \text{I}$ ) as a function of temperature. As shown in Figure 4d, magnetic moments of monolayer CrSeCl, CrSeBr, and CrSeI decrease to zero when the temperature increase to 350, 360, and 385 K, respectively, which indicates that the Curie temperatures of monolayer CrSeCl, CrSeBr, and CrSeI are 350, 360, and 385 K, respectively (Figure 4e). Their Curie temperatures are much higher than those of monolayer  $\text{CrI}_3$  and  $\text{Cr}_2\text{Ge}_2\text{Te}_6$  (45 and 20 K). Therefore, from the Curie temperatures, monolayer CrSeX ( $X = \text{Cl}, \text{Br}, \text{I}$ ) species are promising candidates for applications in spintronic devices.

Finally, the MAE of monolayer CrSeX ( $X = \text{Cl}, \text{Br}, \text{I}$ ) is investigated in depth. Figure 5a–c shows the variation of total MAE and MAE of each atom as a function of angle  $\theta$ , where the angle  $\theta$  ranges from 0 to  $180^\circ$  for monolayer CrSeCl, CrSeBr, and CrSeI. As shown in Table 2, when  $\theta$  is equal to  $0^\circ$  and  $90^\circ$ , the total MAE of monolayer CrSeCl, CrSeBr, and CrSeI are  $-0.199$  and  $0.087$  meV/unit,  $-0.504$  and  $-0.099$  meV/unit cell, and  $0.951$  and  $2.206$  meV/unit cell, respectively. Combined with the data in Figure 5, it is concluded that a strong PMA can be obtained in monolayer CrSeI, while monolayer CrSeCl and CrSeBr possess weak in-plane magnetic anisotropy and their easily magnetized direction is the [100] axis. Furthermore, Table 2 shows that

the PMA of monolayer CrSeI is mainly provided by nonmetallic I atoms, and the contributions of Cr and Se atoms to the total MAE of monolayer CrSeCl and CrSeBr are small. Interestingly, PMA of the nonmetallic I atom reaches up to 0.572 meV per atom in the case of angle  $\theta = 90^\circ$ , which is comparable to that of metallic Fe atoms at Fe/MgO interfaces.<sup>70</sup> As known, the magnetic anisotropy originates from the SOC, and the strength of the SOC is proportional to the fourth power of the atomic number. Therefore, with increasing atomic number (Cl to I), I atoms with large SOC can provide large contributions to strong PMA of monolayer CrSeI. Also it can be seen from Table 2 and Figure 5c that the energy of monolayer CrSeI for the magnetic moment aligning [100] axis is smaller than the energy for the magnetic moment aligning [010] axis. Here, we take  $\theta = 0^\circ$  and  $90^\circ$  as examples to elucidate the strong PMA of monolayer CrSeI induced by nonmetallic I atoms. Figure 6a,b shows the p-orbital-resolved MAEs of the nonmetallic I atom in monolayer CrSeI when  $\theta$  is equal to  $0^\circ$  and  $90^\circ$ , respectively. As shown in Figure 6a, the PMA of monolayer CrSeI is mainly provided by the matrix element difference ( $p_x, p_y$ ) of the nonmetallic I atoms, while ( $p_y, p_z$ ) provides a negative contribution to the PMA when  $\theta$  is equal to  $0^\circ$ . Moreover, the positive contribution of the matrix elements difference ( $p_x, p_y$ ) to the PMA of monolayer CrSeI is larger than the negative contribution of ( $p_y, p_z$ ); thus the MAE of monolayer CrSeI is positive when  $\theta$  is equal to  $0^\circ$ . In contrast, when  $\theta$  is equal to  $90^\circ$ , the matrix element difference ( $p_x, p_y$ ) provides a large positive to the PMA of monolayer CrSeI, while the contributions of ( $p_y, p_z$ ) are almost zero. As a result, the PMA of monolayer CrSeI in the case of  $\theta = 90^\circ$  is obviously larger than that in the case of angle  $\theta = 0^\circ$ . Also the negative contribution of the matrix element difference ( $p_y, p_z$ ) of the nonmetallic I atoms to the MAE in the case of  $\theta = 0^\circ$  leads to lower energy of monolayer CrSeI for the magnetic moment aligning the [100] axis compared to energy for the magnetic moment aligning the [010] axis.

On the basis of second-order perturbation theory, we qualitatively explain the origin of the PMA energy of the monolayer CrSeI by analyzing the projected DOS of the p-orbital of the nonmetallic I atom. As depicted in Figure 6c, the most occupied states of the nonmetallic I atom near the Fermi level are the spin-up  $p_y$  states and the most unoccupied states of the nonmetallic I atom near the Fermi level are spin-up  $p_z$  and  $p_x$  states. Therefore, according to eq 7, we only discuss the contribution to the MAE from the matrix element differences between occupied spin-up and unoccupied spin-up p states of the nonmetallic I atom. Table 3 lists the matrix element differences between occupied spin-up and unoccupied spin-up p orbitals. As listed in Table 3,  $(p_x^+, p_y^+) = 1$  and  $(p_y^+, p_z^+) = -1$  in the case of  $\theta = 0^\circ$ . As a result, the matrix element difference ( $p_x^+, p_y^+$ ) of the nonmetallic I atoms provides a positive contribution to the PMA, while ( $p_y^+, p_z^+$ ) provides a negative contribution to the PMA when  $\theta$  is equal to  $0^\circ$ , as shown in

Figure 6a. In contrast,  $(p_x^+, p_y^+) = 1$  and  $(p_y^+, p_z^+) = 0$  in the case of  $\theta = 90^\circ$ . Therefore, when  $\theta$  is equal to  $90^\circ$ , the matrix element difference ( $p_x^+, p_y^+$ ) provides a large positive to the PMA of monolayer CrSeI, while the contributions of ( $p_y^+, p_z^+$ ) are almost zero; thus the PMA of monolayer CrSeI in the case of  $\theta = 90^\circ$  is obviously larger than that in the case of angle  $\theta = 0^\circ$ . Meanwhile the difference of ( $p_y^+, p_z^+$ ) in the case of  $\theta = 0^\circ$  and  $90^\circ$  also is the reason why the energy of monolayer CrSeI for the magnetic moment aligning [100] axis is smaller than the energy for the magnetic moment aligning [010] axis.

## 4. CONCLUSIONS

In summary, monolayer CrSeX (X = Cl, Br, I) can be prepared from bulk structures and show good dynamic and thermal stability. It is worth noting that monolayer CrSeX (X = Cl, Br, I) species are 2D intrinsic ferromagnetic semiconductors and their Curie temperatures can reach or even exceed room temperature. More importantly, monolayer CrSeI also has higher PMA energy, reaching as high as 0.572 meV per atom, which is mainly due to the spin-polarized p-orbitals of nonmetallic I atoms. In contrast, monolayer CrSeCl and CrSeBr possess weak in-plane magnetic anisotropy and their easily magnetized direction is the [100] axis. By analyzing the projected density of states and the p-orbital-resolved MAE of the nonmetallic I atom based on second-order perturbation theory, we found that the large PMA energy of monolayer CrSeI is mainly the result of the matrix element difference between spin-up  $p_x$  and  $p_y$  states of the I atom, and difference between it and the matrix element difference between spin-up  $p_y$  and  $p_z$  states of the I atom in the case of  $\theta = 0^\circ$  and  $90^\circ$  is the reason why the energy of monolayer CrSeI for the magnetic moment aligning [100] axis is smaller than the energy for the magnetic moment aligning [010] axis. These results indicate that the high Curie temperature and strong PMA may be obtained in 2D intrinsic ferromagnet in the future.

## ■ AUTHOR INFORMATION

### Corresponding Author

Ruilin Han – School of Physics and Electronic Engineering, Shanxi University, Taiyuan 030006, China;  [orcid.org/0000-0002-8325-4748](https://orcid.org/0000-0002-8325-4748); Email: hanruilin0116@sxu.edu.cn

### Authors

Zhou Jiang – Key Laboratory of Material Modification by Laser, Ion and Electron Beams, Ministry of Education, Dalian University of Technology, Dalian 116024, China

Yu Yan – Key Laboratory of Physics and Technology for Advanced Batteries, Ministry of Education, Department of Physics, Jilin University, Changchun 130012, China;  [orcid.org/0000-0002-1316-9783](https://orcid.org/0000-0002-1316-9783)

Complete contact information is available at:  
<https://pubs.acs.org/10.1021/acs.jpcc.0c01307>

### Notes

The authors declare no competing financial interest.

## ■ ACKNOWLEDGMENTS

This work was supported by the National Natural Science Foundation of China (Grant Nos. 11747102 and 11874173) and the Natural Science Young Foundation of Shanxi Province (Grant No. 201901D211190). The work was carried out at the

**Table 3. Matrix Element Differences between Two Magnetization Directions in Eq 7 ( $\langle o^+ | L_z | u^+ \rangle^2 - \langle o^+ | L_\theta | u^+ \rangle^2$ )**

$u^+$	$o^+$		
	$p_y$	$p_z$	$p_x$
$p_y$	0	$-\cos^2\theta$	1
$p_z$	$-\cos^2\theta$	0	$-\sin^2\theta$
$p_x$	1	$-\sin^2\theta$	0

National Supercomputer Center in Tianjin, and the calculations were performed on TianHe-1(A).

## ■ REFERENCES

- (1) Novoselov, K. S.; Geim, A. K.; Morozov, S. V.; Jiang, D.; Zhang, Y.; Dubonos, S. V.; Grigorieva, I. V.; Firsov, A. A. Electric Field Effect in Atomically Thin Carbon Films. *Science* **2004**, *306*, 666–669.
- (2) Li, L. K.; Yang, F. Y.; Ye, G. J.; Zhang, Z. C.; Zhu, Z. W.; Lou, W. K.; Zhou, X. Y.; Li, L.; Watanabe, K.; Taniguchi, T.; et al. Quantum Hall effect in black phosphorus two-dimensional electron system. *Nat. Nanotechnol.* **2016**, *11*, 593–597.
- (3) Xu, M.; Liang, T.; Shi, M.; Chen, H. Graphene-like two-dimensional materials. *Chem. Rev.* **2013**, *113*, 3766–3798.
- (4) Miao, N. H.; Xu, B.; Bristowe, N. C.; Zhou, J.; Sun, Z. M. Tunable magnetism and extraordinary sunlight absorbance in indium triphosphide monolayer. *J. Am. Chem. Soc.* **2017**, *139*, 11125–11131.
- (5) Li, B.; Xing, T.; Zhong, M.; Huang, L.; Lei, N.; Zhang, J.; Li, J.; Wei, Z. M. A two-dimensional Fe-doped SnS<sub>2</sub> magnetic semiconductor. *Nat. Commun.* **2017**, *8*, 1958.
- (6) Zhang, J. M.; Zheng, H. L.; Han, R. L.; Du, X. B.; Yan, Y. Tuning magnetic properties of CrS<sub>2</sub> monolayer by doping transition metal and alkaline-earth atoms. *J. Alloys Compd.* **2015**, *647*, 75–81.
- (7) Li, J.; Zhao, B.; Chen, P.; Wu, R. X.; Li, B.; Xia, Q. L.; Guo, G. H.; Luo, J.; Zang, K. T.; Zhang, Z. W.; et al. Synthesis of ultrathin metallic MTe<sub>2</sub> (M= V, Nb, Ta) single-crystalline nanoplates. *Adv. Mater.* **2018**, *30*, 1801043.
- (8) Tan, C. L.; Cao, X. H.; Wu, X. J.; He, Q. Y.; Yang, J.; Zhang, X.; Chen, J. Z.; Zhao, W.; Han, S. K.; Nam, G. H.; et al. Recent advances in ultrathin two-dimensional nanomaterials. *Chem. Rev.* **2017**, *117*, 6225–6331.
- (9) Zheng, H. L.; Yang, B. S.; Wang, D. D.; Han, R. L.; Du, X. B.; Yan, Y. Tuning magnetism of monolayer MoS<sub>2</sub> by doping vacancy and applying strain. *Appl. Phys. Lett.* **2014**, *104*, 132403.
- (10) O'Hara, D. J.; Zhu, T. C.; Trout, A. H.; Ahmed, A. S.; Luo, Y. K.; Lee, C. H.; Brenner, M. R.; Rajan, S.; Gupta, J. A.; McComb, D. W.; Kawakami, R. K. Room Temperature Intrinsic Ferromagnetism in Epitaxial Manganese Selenide Films in the Monolayer Limit. *Nano Lett.* **2018**, *18*, 3125–3131.
- (11) Mermin, N. D.; Wagner, H. Absence of Ferromagnetism or Antiferromagnetism in One- or Two-Dimensional Isotropic Heisenberg Models. *Phys. Rev. Lett.* **1966**, *17*, 1133–1136.
- (12) Huang, B.; Clark, G.; Navarro-Moratalla, E.; Klein, D. R.; Cheng, R.; Seyler, K. L.; Zhong, D.; Schmidgall, E.; McGuire, M. A.; Cobden, D. H.; et al. Layer-Dependent Ferromagnetism in a Van Der Waals Crystal Down to the Monolayer Limit. *Nature* **2017**, *546*, 270–273.
- (13) Tian, Y.; Gray, M. J.; Ji, H.; Cava, R. J.; Burch, K. S Magneto-elastic coupling in a potential ferromagnetic 2D atomic crystal. *2D Mater.* **2016**, *3*, 025035.
- (14) Ma, X. F.; Mi, W. B. Surface Functionalization Tailored Electronic Structure and Magnetic Properties of Two-Dimensional Cr<sub>2</sub>C Monolayers. *J. Phys. Chem. C* **2020**, *124*, 3095–3106.
- (15) Zhang, W.; Guo, H. T.; Jiang, J.; Tao, Q. C.; Song, X. J.; Li, H.; Huang, J. Magnetism and magnetocrystalline anisotropy in single-layer PtSe<sub>2</sub>: Interplay between strain and vacancy. *J. Appl. Phys.* **2016**, *120*, 013904.
- (16) Zhang, F.; Mi, W. B.; Wang, X. C. Spin-Dependent Electronic Structure and Magnetic Anisotropy of 2D Ferromagnetic Janus Cr<sub>2</sub>I<sub>3</sub>X<sub>3</sub> (X = Br, Cl) Monolayers. *Adv. Electron Materi* **2020**, *6*, 1900778.
- (17) Jin, Y. L.; Valloppilly, S.; Kharel, P.; Pathak, R.; Kashyap, A.; Skomski, R.; Sellmyer, D. J. Unusual perpendicular anisotropy in Co<sub>3</sub>TiSi films. *J. Phys. D: Appl. Phys.* **2019**, *52*, 035001.
- (18) Yang, B. S.; Jiang, L. N.; Chen, W. Z.; Tang, P.; Zhang, J.; Zhang, X. – G.; Yan, Y.; Han, X. F. First-principles study of perpendicular magnetic anisotropy in ferromagnetic D0<sub>22</sub>-Mn<sub>3</sub>X (X = Ga, Ge) on MgO and SrTiO<sub>3</sub>. *Appl. Phys. Lett.* **2018**, *112*, 142403.
- (19) Pei, Q.; Zhou, B. Z.; Mi, W. B.; Cheng, Y. C. Triferroic Material and Electrical Control of Valley Degree of Freedom. *ACS Appl. Mater. Interfaces* **2019**, *11*, 12675–12682.
- (20) Yang, H. X.; Vu, A. D.; Hallal, A.; Rougemaille, N.; Coraux, J.; Chen, G.; Schmid, A.; Chshiev, M. Anatomy and Giant Enhancement of the Perpendicular Magnetic Anisotropy of Cobalt–Graphene Heterostructures. *Nano Lett.* **2016**, *16*, 145–151.
- (21) Yang, B. S.; Zhang, J.; Jiang, L. N.; Chen, W. Z.; Tang, P.; Zhang, X. – G.; Yan, Y.; Han, X. F. Strain induced enhancement of perpendicular magnetic anisotropy in Co/graphene and Co/BN heterostructures. *Phys. Rev. B: Condens. Matter Mater. Phys.* **2017**, *95*, 174424.
- (22) Yan, L.; Mi, W. B.; Wang, X. C. Perpendicular Magnetic Anisotropy and High Spin Polarization in Tetragonal Fe<sub>4</sub>N/BiFeO<sub>3</sub> Heterostructures. *Phys. Rev. Appl.* **2016**, *6*, 064022.
- (23) Wen, Z. C.; Sukegawa, H.; Furubayashi, T.; Koo, J.; Inomata, K.; Mitani, S.; Hadorn, J. P.; Ohkubo, T.; Hono, K. A 4-Fold-Symmetry Hexagonal Ruthenium for Magnetic Heterostructures Exhibiting Enhanced Perpendicular Magnetic Anisotropy and Tunnel Magnetoresistance. *Adv. Mater.* **2014**, *26*, 6483–6490.
- (24) Wang, W. G.; Li, M. G.; Hageman, S.; Chien, C. L. Electric-field-assisted switching in magnetic tunnel junctions. *Nat. Mater.* **2012**, *11*, 64–68.
- (25) Cui, Y. S.; Khodadadi, B.; Schafer, S.; Mewes, T.; Lu, J.; Wolf, S. A. Interfacial perpendicular magnetic anisotropy and damping parameter in ultra thin Co<sub>2</sub>FeAl films. *Appl. Phys. Lett.* **2013**, *102*, 162403.
- (26) Vadapoo, R.; Hallal, A.; Yang, H. X.; Chshiev, M. First-principles investigation of magnetocrystalline anisotropy at the L2<sub>1</sub> full Heusler/MgO interfaces and tunnel junctions. *Phys. Rev. B: Condens. Matter Mater. Phys.* **2016**, *94*, 104418.
- (27) Li, F. F.; Yang, B. S.; Zhang, J. M.; Han, X. F.; Yan, Y. Interface-induced perpendicular magnetic anisotropy in Co<sub>2</sub>FeAl/NiFe<sub>2</sub>O<sub>4</sub> superlattice: first-principles study. *Phys. Chem. Chem. Phys.* **2020**, *22*, 716–723.
- (28) Bonilla, M.; Kolekar, S.; Ma, Y.; Diaz, H. C.; Kalappattil, V.; Das, R.; Eggers, T.; Gutierrez, H. R.; Phan, M. H.; Batzill, M. Strong room-temperature ferromagnetism in VSe<sub>2</sub> monolayers on van der Waals substrates. *Nat. Nanotechnol.* **2018**, *13*, 289–293.
- (29) Deng, Y. J.; Yu, Y. J.; Song, Y. C.; Zhang, J. Z.; Wang, N. Z.; Sun, Z. Y.; Yi, Y. F.; Wu, Y. Z.; Wu, S. W.; Zhu, J. Y.; et al. Gate-tunable room-temperature ferromagnetism in two-dimensional Fe<sub>3</sub>GeTe<sub>2</sub>. *Nature* **2018**, *563*, 94–99.
- (30) Yu, W.; Li, J.; Herng, T. S.; Wang, Z. S.; Zhao, X. X.; Chi, X.; Fu, W.; Zhou, J.; et al. Chemically exfoliated VSe<sub>2</sub> monolayers with room-temperature ferromagnetism. *Adv. with room-temperature ferromagnetism. Adv. Mater.* **2019**, *31*, 1903779.
- (31) Long, G.; Zhang, T.; Cai, X. B.; Hu, J.; Cho, C. W.; Xu, S. G.; Shen, J. Y.; Wu, Z. F.; Han, T. Y.; Lin, J. X. Z.; et al. Isolation and Characterization of Few-Layer Manganese Thiophosphate. *ACS Nano* **2017**, *11*, 11330.
- (32) Sun, X. D.; Li, W. Y.; Wang, X.; Sui, Q.; Zhang, T. Y.; Wang, Z.; Liu, L.; Li, D.; Feng, S.; Zhong, S. Y. Room temperature 2D ferromagnetism in few-layered 1T-CrTe<sub>2</sub>. *arXiv* **1909.09797**, 2019, <https://arxiv.org/abs/1909.09797>.
- (33) Wang, B.; Wu, Q. S.; Zhang, Y. H.; Guo, Y. L.; Zhang, X. W.; Zhou, Q. H.; Dong, S.; Wang, J. L. High Curie-temperature intrinsic ferromagnetism and hole doping-induced half-metallicity in two-dimensional scandium chlorine monolayers. *Nanoscale Horiz* **2018**, *3*, 551–555.
- (34) Kulish, V. V.; Huang, W. Single-layer metal halides MX<sub>2</sub> (X = Cl, Br, I): stability and tunable magnetism from first principles and Monte Carlo simulations. *J. Mater. Chem. C* **2017**, *5*, 8734–8741.
- (35) Botana, A. S.; Norman, M. R. Electronic structure and magnetism of transition metal dihalides: Bulk to monolayer. *Phys. Rev. Mater.* **2019**, *3*, 044001.
- (36) Jiang, Z.; Wang, P.; Xing, J. P.; Jiang, X.; Zhao, J. J. Screening and design of novel 2D ferromagnetic materials with high curie

- temperature above room temperature. *ACS Appl. Mater. Interfaces* **2018**, *10*, 39032–39039.
- (37) Guo, Y. L.; Zhang, Y. H.; Yuan, S. J.; Wang, B.; Wang, J. L. Chromium sulfide halide monolayers: intrinsic ferromagnetic semiconductors with large spin polarization and high carrier mobility. *Nanoscale* **2018**, *10*, 18036–18042.
- (38) Huang, C.; Zhou, J.; Wu, H.; Deng, K.; Jena, P.; Kan, E. Quantum Anomalous Hall Effect in Ferromagnetic Transition Metal Halides. *Phys. Rev. B: Condens. Matter Mater. Phys.* **2017**, *95*, 045113.
- (39) Miao, N. H.; Xu, B.; Zhu, L.; Zhou, J.; Sun, Z. M. 2D Intrinsic Ferromagnets from van der Waals Antiferromagnets. *J. Am. Chem. Soc.* **2018**, *140*, 2417–2420.
- (40) Wang, Y. J.; Li, F. F.; Zheng, H. L.; Han, X. F.; Yan, Y. Large magnetic anisotropy and its strain modulation in two-dimensional intrinsic ferromagnetic monolayer RuO<sub>2</sub> and OsO<sub>2</sub>. *Phys. Chem. Chem. Phys.* **2018**, *20*, 28162–28168.
- (41) Zhang, X. W.; Wang, B.; Guo, Y. L.; Zhang, Y. H.; Chen, Y. F.; Wang, J. L. High Curie temperature and intrinsic ferromagnetic half-metallicity in two-dimensional Cr<sub>3</sub>X<sub>4</sub> (X = S, Se, Te) nanosheets. *Nanoscale Horiz.* **2019**, *4*, 859–866.
- (42) Zheng, S.; Huang, C. X.; Yu, T.; Xu, M. L.; Zhang, S. T.; Xu, H. Y.; Liu, Y. C.; Kan, E.; Wang, Y. C.; Yang, G. C. High-Temperature Ferromagnetism in an Fe<sub>3</sub>P Monolayer with a Large Magnetic Anisotropy. *J. Phys. Chem. Lett.* **2019**, *10*, 2733–2738.
- (43) He, J.; Ma, S.; Lyu, P.; Nachtigall, P. Unusual Dirac half-metallicity with intrinsic ferromagnetism in vanadium trihalide monolayers. *J. Mater. Chem. C* **2016**, *4*, 2518–2526.
- (44) Zhou, Y. G.; Lu, H. F.; Zu, X. T.; Gao, F. Evidencing the existence of exciting half-metallicity in two-dimensional TiCl<sub>3</sub> and VCl<sub>3</sub> sheets. *Sci. Rep.* **2016**, *6*, 19407.
- (45) Wu, F.; Huang, C.; Wu, H.; Lee, C.; Deng, K.; Kan, E.; Jena, P. Atomically Thin Transition-Metal Dinitrides: High-Temperature Ferromagnetism and Half-Metallicity. *Nano Lett.* **2015**, *15*, 8277–8281.
- (46) Xu, Z.; Zhu, H. Two-Dimensional Manganese Nitride Monolayer with Room Temperature Rigid Ferromagnetism under Strain. *J. Phys. Chem. C* **2018**, *122*, 14918–14927.
- (47) Wang, B.; Zhang, Y.; Ma, L.; Wu, Q.; Guo, Y.; Zhang, X.; Wang, J. MnX (X = P, As) Monolayers: A New Type of Two Dimensional Intrinsic Room Temperature Ferromagnetic Half-Metallic Material with Large Magnetic Anisotropy. *Nanoscale* **2019**, *11*, 4204–4209.
- (48) Zheng, H. L.; Zheng, J.; Wang, C.; Han, H. C.; Yan, Y. Enhancing the perpendicular magnetic anisotropy of 1T-FeCl<sub>2</sub> monolayer by applying strain: first-principles study. *J. Magn. Magn. Mater.* **2017**, *444*, 184–189.
- (49) Han, R. L.; Yan, Y. Strain-tunable electric structure and magnetic anisotropy in monolayer CrSI. *Phys. Chem. Chem. Phys.* **2019**, *21*, 20892–20900.
- (50) Kresse, G.; Furthmüller, J. Efficient iterative schemes for ab initio total-energy calculations using a plane-wave basis set. *Phys. Rev. B: Condens. Matter Mater. Phys.* **1996**, *54*, 11169–11186.
- (51) Perdew, J. P.; Burke, K.; Ernzerhof, M. Generalized gradient approximation made simple. *Phys. Rev. Lett.* **1996**, *77*, 3865–3868.
- (52) Anisimov, V. I.; Zaanen, J.; Andersen, O. K. Band theory and Mott insulators: Hubbard U instead of Stoner I. *Phys. Rev. B: Condens. Matter Mater. Phys.* **1991**, *44*, 943–954.
- (53) Dudarev, S. L.; Botton, G. A.; Savrasov, S. Y.; Humphreys, C. J.; Sutton, A. P. Electron-energy-loss spectra and the structural stability of nickel oxide: An LSDA+U study. *Phys. Rev. B: Condens. Matter Mater. Phys.* **1998**, *57*, 1505–1509.
- (54) Huang, C. X.; Feng, J. S.; Wu, F.; Ahmed, D.; Huang, B.; Xiang, H. J.; Deng, K. M.; Kan, E. Toward Intrinsic Room-Temperature Ferromagnetism in Two-Dimensional Semiconductors. *J. Am. Chem. Soc.* **2018**, *140*, 11519–11525.
- (55) Chadi, D. J. Special points for Brillouin-zone integrations. *Phys. Rev. B* **1977**, *16*, 1746–1747.
- (56) Togo, A.; Tanaka, I. First principles phonon calculations in materials science. *Scr. Mater.* **2015**, *108*, 1–5.
- (57) Martyna, G. J.; Klein, M. L.; Tuckerman, M. Nosé–Hoover chains: The canonical ensemble via continuous dynamics. *J. Chem. Phys.* **1992**, *97*, 2635–2643.
- (58) Liu, Z. F.; Liu, J. Y.; Zhao, J. J. YN<sub>2</sub> monolayer: Novel p-state Dirac half metal for high speed spintronics. *Nano Res.* **2017**, *10*, 1972–1979.
- (59) Hu, J.; Wu, R. Control of the Magnetism and Magnetic Anisotropy of a Single-Molecule Magnet with an Electric Field. *Phys. Rev. Lett.* **2013**, *110*, 097202.
- (60) Wang, X. D.; Wu, R. Q.; Wang, D.-S.; Freeman, A. J. Torque method for the theoretical determination of magnetocrystalline anisotropy. *Phys. Rev. B: Condens. Matter Mater. Phys.* **1996**, *54*, 61–64.
- (61) Wang, D. S.; Wu, R. Q.; Freeman, A. J. First-Principles Theory of Surface Magnetocrystalline Anisotropy and the Diatomic-Pair Mode. *Phys. Rev. B: Condens. Matter Mater. Phys.* **1993**, *47*, 14932–14947.
- (62) Beck, J. Über Chalkogenidhalogenide des Chroms Synthese, Kristallstruktur und Magnetismus von chromiumsulfidebromid, CrSBr. *Z. Anorg. Allg. Chem.* **1990**, *585*, 157–167.
- (63) Katscher, H.; Hahn, H. Über Chalkogenidhalogenide des dreiwertigen Chroms. *Naturwissenschaften* **1966**, *53*, 361.
- (64) Jung, J. H.; Park, C.-H.; Ihm, J. A Rigorous Method of Calculating Exfoliation Energies from First Principles. *Nano Lett.* **2018**, *18*, 2759–2765.
- (65) Zacharia, R. J.; Ulbricht, H.; Hertel, T. Interlayer cohesive energy of graphite from thermal desorption of polyaromatic hydrocarbons. *Phys. Rev. B: Condens. Matter Mater. Phys.* **2004**, *69*, 155406.
- (66) Ziambaras, E.; Kleis, J.; Schröder, E.; Hyldgaard, P. Potassium intercalation in graphite: A van der Waals density-functional study. *Phys. Rev. B: Condens. Matter Mater. Phys.* **2007**, *76*, 155425.
- (67) Anderson, P. W. New Approach to the Theory of Superexchange Interactions. *Phys. Rev.* **1959**, *115*, 2–13.
- (68) Goodenough, J. B. Theory of the Role of Covalence in the Perovskite-Type Manganites [La, M(II)] MnO<sub>3</sub>. *Phys. Rev.* **1955**, *100*, S64–S73.
- (69) Kanamori, J. Crystal distortion in magnetic compounds. *J. Appl. Phys.* **1960**, *31*, S14–S23.
- (70) Yang, H. X.; Chshiev, M.; Dieny, B.; Lee, J. H.; Manchon, A.; Shin, K. H. First-Principles Investigation of the Very Large Perpendicular Magnetic Anisotropy at Fe/MgO and Co/MgO Interfaces. *Phys. Rev. B: Condens. Matter Mater. Phys.* **2011**, *84*, 054401.